AIP Advances

Phonon thermal transport in copper: The effect of size, crystal orientation, and grain boundaries

Cite as: AIP Advances **12**, 065301 (2022); https://doi.org/10.1063/5.0094170
Submitted: 01 April 2022 • Accepted: 06 May 2022 • Published Online: 01 June 2022

Sandra Sæther, Merete Falck Erichsen, Senbo Xiao, et al.

View Online
Export Citation
CrossMark

© 2022 Author(s).

Phonon thermal transport in copper: The effect of size, crystal orientation, and grain boundaries

Cite as: AIP Advances 12, 065301 (2022); doi: 10.1063/5.0094170
Submitted: 1 April 2022 • Accepted: 6 May 2022 •
Published Online: 1 June 2022

View Online Export Citation CrossMark

Sandra Sæther,[1] Merete Falck Erichsen,[1] Senbo Xiao,[1] Zhiliang Zhang,[1] Anders Lervik,[2] and Jianying He[1,a)]

AFFILIATIONS

[1] Department of Structural Engineering, Faculty of Engineering, Norwegian University of Science and Technology (NTNU), 7491 Trondheim, Norway
[2] Department of Chemistry, Faculty of Natural Sciences, Norwegian University of Science and Technology (NTNU), 7491 Trondheim, Norway

[a)] **Author to whom correspondence should be addressed:** jianying.he@ntnu.no

ABSTRACT

In electronic devices at the micro- and nanoscale, thermal management is vital. At such small sizes, crystal orientation, grain boundaries, and even the size itself can play an important role in the thermal transport and need to be taken into careful consideration when devices are designed. In this article, we perform computational experiments using non-equilibrium molecular dynamics simulations to evaluate the effect of size, orientation, and grain boundaries on the phonon thermal transport of copper. In addition, we compare the results obtained from the rescale and Langevin thermostat procedures. We find that the contribution of phonons to the total thermal conductivity in copper increases as the size decreases. Furthermore, the Σ5(210)[001] twist grain boundary is found to have a significant effect on the thermal transport of a bi-crystalline copper system when the grains are 15 nm. No such effect is found for the Σ3(112)[110] twin boundary. The effect of crystal orientation on the thermal conductivity is also studied, and no discerned effect can be observed. It is found that the Langevin thermostat leads to an over-estimation of the thermal conductivities at smaller scales and should be used with caution.

© 2022 Author(s). All article content, except where otherwise noted, is licensed under a Creative Commons Attribution (CC BY) license (http://creativecommons.org/licenses/by/4.0/). https://doi.org/10.1063/5.0094170

I. INTRODUCTION

With electronic devices dropping to the micro- and nanoscale, thermal management is becoming a vital aspect of development, as this minimization of systems is causing an increase in heat accumulation. This, in turn, leads to a reduced lifespan of devices. It is, therefore, crucial to understand the factors that influence heat transmission in different materials. Of particular importance are metallic nanofilms and nanowires as they play a critical role in electronic applications.

The existence of a size effect in the thermal conductivity of materials is well established. When the length scale of systems becomes lower than the mean free path of heat carriers, the thermal conductivity becomes lower than the bulk value.[4] This decrease in thermal conductivity is attributed to scattering, either on the surface or on the grain boundaries of the material.[6]

In order to describe the effect of these scattering events on transport properties, several theories and models have been developed for electrons. A common method is to apply the Boltzmann transport equation (BTE) with the relaxation time approximation (RTA), the Fuchs–Sonderheim theory for boundary scattering,[14,33] and the Mayadas–Shatzkes theory for grain boundary scattering.[24] These theories are also used for describing phonon transport. In that case, it is often assumed that the phonons are not scattered at grain boundaries, i.e., that the reflection coefficient in Mayadas–Shatzkes model is zero.[19,34]

Another way to estimate the phonon transport is to use Molecular Dynamics simulations (MD), in which Fourier's law can be used to investigate the phonon thermal conductivity. As Fourier's law can be obtained from the BTE under the RTE approximation by assuming local equilibrium, these methods include some of the same assumptions. As MD simulations are based on interatomic

© Author(s) 2022

potentials, assumptions required to solve the BTE analytically do not have to be made, and as anharmonicity is inherently built in the potentials, inelastic effects due to multiple phonon interactions are included.[15] Non-Equilibrium Molecular dynamics (NEMD) simulations have been widely used to study the thermal transport of different systems.[3,5,11,13,17,20,31] As long as the systems are in the linear-response regime, NEMD simulations can be used to gain insight into the thermal transport process. The underlying assumption of NEMD simulations, specifically that there is local equilibrium in small regions of the system, has been shown to be valid even at high temperature gradients and for a small number of particles in the control volume.[16]

How large of an influence the phonon thermal conductivity has on the overall thermal conductivity of metals is under debate, and a definite understanding of the different factors influencing the phonon thermal transport is lacking.[19] There is no predictable trend on how metal shrinking is going to influence the phonon contribution to the total thermal transport. However, it has been shown by several researchers that the Lorentz ratio of the Wiedemann–Franz law deviates from the Sommerfeld value at small scales, meaning that the phonon contribution to the thermal conductivity becomes significant.[19,34] Hu *et al.* suggested that the phonon contribution to the total thermal conductivity will increase with decreasing sizes for metals where the phonon thermal conductivity is small for the bulk system. For systems where the phonon contribution to the bulk is large, they predict that the decrease in size can either lead to an increase or a suppression of the phonon thermal conductivity to the total thermal conductivity.[19]

Copper used in integrated circuits is polycrystalline, consisting of grains with various crystallographic orientations.[2] When studying thermal transport, the effect of grain boundary scattering of phonons is modeled as a probability, and as previously mentioned, it is often assumed that the phonon thermal transport is not influenced by the grain boundary at all, due to the long phonon wavelength in comparison to the dimension of the grain.[19,34] However, there exists a vast number of different types of grain boundaries, and to the authors' knowledge, the effect of these on phonon thermal transport has thus far not been tested. In this paper, two commonly occurring grain boundaries, a Σ3 twin boundary and a Σ5 twist boundary will, therefore, be investigated to see if this assumption holds for copper.

All atomic positions in an fcc structure are equivalent, and thus, the atomic displacements are isotropic in pure fcc crystals such as copper.[25] However, this does not mean that the material properties are isotropic, due to the inherent anisotropy of the unit cell. An example of this is the elastic modulus, which varies substantially for the different crystallographic orientations. For instance, the elastic modulus for the [100] direction is three times smaller than the elastic modulus for the [111] direction.[1,2] It is of importance to investigate whether or not this anisotropy can also be seen in the heat transport of the crystal, as this will have an effect on the overall heat transport on smaller scales, such as metal lines in integrated circuits. The effect of crystal orientation on the phonon thermal transport will, therefore, also be studied.

This paper is structured as follows: in Sec. II, the simulation models and methods are presented, and details of the data analysis used to characterize the interface are presented. In Sec. III, the results are presented and discussed, and Sec. IV contains the summary and conclusions of our study.

II. SIMULATION MODELS AND METHODS

A. Simulation details

In order to study the heat transfer in the different copper systems, boundary-driven NEMD simulations were carried out. The explicit temperature gradients were created by thermostatting different regions of the simulation boxes. All simulations are performed using the LAMMPS (Large-scale Atomic/Molecular Massively Parallel Simulator) software.[29] The Embedded Atom Method (EAM) potential of Mishin *et al.* is used to describe the forces between the atoms, as it has been verified for thermal properties.[11,26] In addition, it accurately reproduces phonon frequencies and elastic constants.[11] In the EAM, each individual atom is embedded into the environment consisting of the other atoms, and it is assumed that the embedding energy of this placement is a function of the local electron density, in addition to the pair wise interaction between the embedded atom and the rest of the system, as expressed in the following equation:

$$E_i = F_\alpha\left(\sum_{j\neq i}\rho_\alpha(r_{ij})\right) + \frac{1}{2}\sum_{j\neq i}\phi_{\alpha\beta}(r_{ij}), \tag{1}$$

where r_{ij} is the distance between atoms i and j, $\phi_{\alpha\beta}$ is a pair-wise potential function, ρ_α is the contribution to the electron charge density from atom j of type α at the location of atom i, and F is an embedding function that represents the energy required to place atom i of type α into the electron cloud created by the other atoms.[7] The multi-body inclusion of this method is a result of the embedding term.[8]

For the study of the size effect and possible anisotropy in the thermal transport, the systems were initialized as ideal fcc crystals with $x \times y$ dimensions of ~7.23 × 7.23 nm^2 (20 unit cells in each direction) and z ranging from ~10 nm to ~80 nm (30–222 unit cells). In order to study the effect of crystal direction, the systems were created with the z-axis oriented in the [111], [110], [001], or [201] direction. The smallest system consisted of 48 800 atoms, and the largest system consisted of 356 000 atoms. The NVT ensemble [obtained with a Nose–Hoover thermostat as implemented in LAMMPS] and a timestep of 1 fs were used, with a shrink-wrapped boundary in the z-direction and periodic boundary conditions utilized for the x and y directions. All systems were equilibrated for 1 ns at 412 K, with the equations of motion being integrated using the Velocity–Verlet integrator as implemented in LAMMPS. After the equilibration, the NEMD simulation was initialized. The thermostated regions were defined at the ends of the simulation box in the z-dimension, with a thickness of ~1.5 nm. This resulted in ~7200 atoms in each of the thermostated regions. The temperature was set to T_h = 425 K on the hot side, and T_c = 400 K on the cold side, and two separate rescale thermostats as implemented in LAMMPS were used to control the temperature in these regions. The NEMD setup of the system is visualized in Fig. 1. Before a production run of 6 ns, the systems were run with the thermostats turned on for a minimum of 6 ns in order to reach a steady state. For the smallest system, five independent production runs were made using the rescale thermostats, with different seeds for generating initial velocities corresponding to the starting temperature of 412 K, in order to evaluate the effect on the uncertainty. For the remaining systems, three independent production runs were made for each system. As

© Author(s) 2022

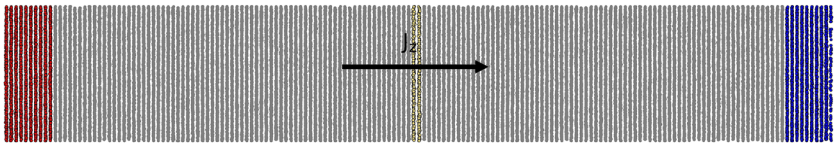

FIG. 1. Computational setup illustrated by 50 000 atoms from the Σ5 system. The red region indicates the area where the hot thermostat is applied, with a temperature of 425 K, and the blue area where the cold thermostat is applied, with a temperature of 400 K. The boundary is colored yellow. In the gray region, the thermal gradient is established. The direction of the heat flux is indicated by an arrow.

this did not result in any noticeable difference in the uncertainty, no additional simulations were run, and the reported results are generated from these three production runs. In addition to this, the effect of using a different thermostat was investigated for the [001] direction, where two separate Langevin thermostats were also tested with a damp parameter of 1.0 fs. For all these systems, five production runs were done for all but the three largest systems.

To investigate the grain boundary thermal resistance, two boundaries were studied: a Σ3(112)[110] coherent twin boundary with a misorientation angle of 70.75° and a Σ5(201)[001] twist boundary with a misorientation angle of 53.13°. The Σ5 boundaries were created by constructing two separate crystals of dimensions $(x \times y)$ of 7.27 × 7.27 nm^2 oriented in the $[02\bar{1}] \times [012]$ and $[021] \times [0\bar{1}2]$ xy-plane, respectively, and joining them along a plane normal to the z-direction. The Σ3 twin boundaries were constructed by joining two crystals oriented in the [111] and $[\bar{1}\bar{1}1]$ directions along the z-axis. Two different grain sizes in the z-direction were simulated: each grain ~15 nm, resulting in systems of around 129 000 atoms, and each grain ~65 nm, resulting in systems of around 589 700 atoms. After this construction, all overlapping atoms were removed, and the systems were equilibrated for 0.1 ns in an NVT ensemble at 412 before the conjugate gradient method was applied. The systems were then allowed to relax in the z-direction, the conjugant gradient method was applied again, and the systems were run for 1 ns in an NPT ensemble. After this, the system was run for 1 ns at 412 K in the NVT ensemble before the thermostats were turned on, and the systems were run for a minimum of 12 ns before a production run of 6 ns. For the (65 × 65) systems, the thermostated regions were set to a thickness of 2 nm, while the (15 × 15) systems were kept at a thermostated region of 1.5 nm. The plotted data from the equilibration and production runs can be found in the supplementary material, Sec. 1.

B. Data processing

The systems were divided into 100 bins in order to obtain the temperature profile from the production runs, with some exceptions. The two smallest systems for the size effect study, namely the 10.8 and 14.7 nm systems, were divided into 20 bins due to noise in the data. The (65 × 65) Σ3 boundary system was divided into 200 bins, as the interface of that system disappeared in the data otherwise. Each bin contained a minimum of 800 atoms. The data points were averaged every 1000 000 steps. The raw data from all runs were then collected and averaged, and the analysis was performed on the ensemble-averaged data for all except the boundary systems. In this case, the boundary was characterized, and the interfacial thermal conductance, G, was found for each run. The reported value for G is, therefore, an average of these.

In the stationary state, the lattice thermal conductivity, κ, is found by assuming that the heat transfer obeys Fourier's law, as outlined in the introduction. For a simulation set up as the one displayed in Fig. 1, with a one-dimensional heat transfer in the z-direction, Fourier's law becomes

$$\kappa = -\frac{J_q}{(dT/dz)}, \tag{2}$$

where J_q is the flux and dT/dz is the corresponding temperature gradient. The heat flux in the simulation is given by

$$J_q = \pm \frac{\langle E_{\text{kin}} \rangle}{\delta t \times A}, \tag{3}$$

where $\langle E_{\text{kin}} \rangle$ is the ensemble average of the kinetic energy enforced on the system, δt is the simulation time step, and A is the cross-sectional area perpendicular to the heat flux. The heat flux for the system was found by performing a linear least squares fit of the average kinetic energy added/subtracted to the system against the simulation time. The temperature gradient, dT/dz, for a given system was found by fitting the ensemble-averaged data for all runs with linear least square regression. This was then used to find the overall thermal conductivities of the systems.

Between regions of different orientations, a Kapitza resistance, R, can be obtained and used to quantify the grain boundary resistance as follows:

$$R = \frac{\Delta T}{J_q}, \tag{4}$$

where ΔT is the temperature discontinuity across the interfacial region.[4] The interfacial conductance, G, is defined as

$$G = \frac{1}{R}. \tag{5}$$

The interfacial conductance was found by extrapolating the linear dependence $T(z)$ from linear fits performed in regions away from the thermostat and interface to the boundaries of the interface, as displayed in Fig. 5 for the Σ3-15 nm twin boundary and Fig. 6 for the Σ5-15 nm twist boundary. The interface was defined through the Common Neighbor Analysis[12,18] as implemented in OVITO.[35] This was done by tracking the atoms defined as "not fcc" every 500 000 time step over the production run and classifying the atoms that consistently belonged to this category as the boundary.

© Author(s) 2022

The uncertainty in all values reported was found through the propagation of errors, with the assumption that the value of the heat flux and the slope of the temperature gradient is uncorrelated. This should hold for the temperature differences considered in this study, as no phase transition occurs. The derivation of this is included in the supplementary material, Sec. 2.

III. RESULTS AND DISCUSSION

A. Crystal orientation

At bulk sizes, copper is a polycrystalline material, consisting of many small crystals with different crystallographic orientations. At this size, all properties are isotropic due to the randomness of these orientations, but at smaller scales, the inherent anisotropy of the specific grains can be seen. As mentioned in the introduction, it is known that the elasticity of copper depends on the crystal orientation.[1,2] This can be seen from the stiffness matrix for FCC crystals.[9] This may suggest a similar effect for phonon transport, as the phonon group velocity for the different directions can be represented by the elastic waves in the given direction for the cubic crystals.[22] This introduces the approximation that acoustic phonons are responsible for thermal transport.[32] By taking the average group velocity as

$$v_{ac} = \frac{v_{ac,L} + v_{ac,T1} + v_{ac,T2}}{3}, \tag{6}$$

where $v_{ac,L}$, $v_{ac,T1}$, and $v_{ac,T2}$ are the velocity of the longitudinal and two transverse modes, and the group velocities for the three lowest index planes are found by using material constants from the work of Evteev *et al.* and are presented in Table I.[11]

It is significant to explore if this has any influence on thermal transport, as this could guide the design of small-scale devices. Four low-index planes (001), (110), (111), and (201) with length from 10 to 80 nm were considered. The results from the investigation of orientation dependent phonon thermal transport are presented in Fig. 2. As can be observed, all grain orientations show a size effect, similar to the electron-based thermal conductivity.[34] Interestingly, the phonon thermal conductivity in different grain orientations nearly overlaps at all lengths, except for a slight deviation for the lengths 10 and 65 nm. No trend can, therefore, be discerned for the effect of crystal orientation on the phonon thermal conductivity.

It should be noted that the EAM potential used in this study accounts for an electronic contribution to the bulk lattice properties relevant to phonon scattering processes through the fitting of the EAM potential and thus can well predict the kinetic properties of copper. We can, therefore, conclude that the phonon heat transport in copper shows no discerned effect dependent on the crystal orientation. According to these results, the orientation of ideal or near-ideal crystals should, therefore, not be of concern in the fabrications of Cu metallic nanofilms and nanowires used for heat transport purposes.

TABLE I. The average group velocities for the [111], [110], and [100] directions of a FCC Cu crystal.

Direction	[111]	[110]	[100]
Velocity (ms^{-1})	2960	3174	3396

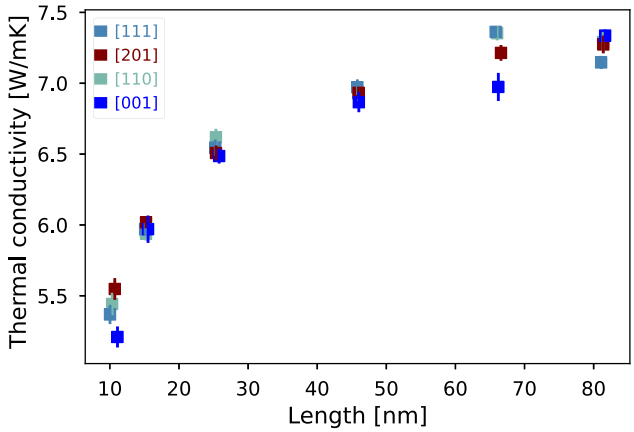

FIG. 2. Lattice thermal conductivity for the four different lattice orientations in the heat flux direction tested in this study, [001], [111], [201], and [110], at different lengths. The error bars are obtained through the propagation of errors, as explained in Sec. II B.

B. Size effect and the effects of thermostats

From the results presented in Fig. 2, a clear size effect can be observed, with the thermal conductivity increasing by about 30% from the smallest to the largest system. It is apparent that the lattice thermal conductivity has a strong size dependence for lengths below 30 nm, whereas, at larger lengths, the growth in thermal conductivity decreases, and a constant value seems to be reached at lengths above 60 nm, where the value for the thermal conductivity becomes nearly independent of the length and stabilizes. For two of the directions, [110] and [111], the value of the lattice thermal conductivity obtained at 65 nm is slightly higher than the value at 80 nm, suggesting that the values are oscillating around a final value.

A much utilized method to estimate the bulk lattice thermal conductivity from NEMD simulations is to plot the thermal conductivity against the inverse length and extrapolate to zero, as displayed in Fig. 3(a). From this, the bulk lattice thermal conductivity is estimated to be 7.49 ± 0.35 W/mK. The largest value of κ obtained in this work (65 nm, [111] direction) was 7.36 ± 0.04, meaning that roughly 98% of the bulk lattice thermal conductivity estimated through this method is reached at this length. This method is intended for systems where the bulk value has not been reached but where the system size is large enough to capture all the long-ranging wavelengths. Schemes have been made in order to estimate if the box size is large enough for this method to be used. Sellan *et al.* proposed the following criteria:

$$\kappa_{\infty}^{\max} = \frac{L k_B v_{ac}}{6a^3}, \tag{7}$$

where L is the length of the system, k_B is Boltzmann's constant, v_{ac} is the acoustic group velocity, and a is the lattice spacing.[32] Linear extrapolation can then be used if $\kappa_{\infty}^{\max}$ is larger than the phonon

© Author(s) 2022

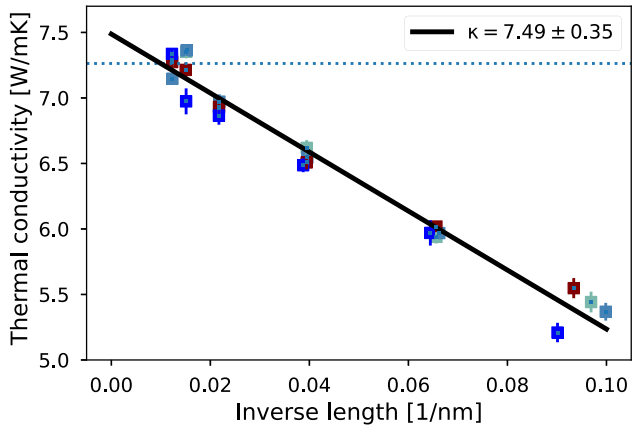

FIG. 3. The thermal conductivity can be estimated in two ways. In (a), the lattice thermal conductivity is plotted vs the inverse length of the system in the z-direction to estimate the bulk lattice thermal conductivity. The value of the estimated thermal conductivity is given in the legend. The light blue, dotted line is the bulk thermal conductivity obtained in (b), which is included for comparison. In (b), the lattice thermal conductivity is plotted vs the length of the system in the z-direction, and fitted with an exponential function. The value of *a*, *b*, and *c* is 7.25, 3.40, and −0.06, respectively. The light blue, dotted line is the obtained bulk thermal conductivity.

thermal conductivity value found from extrapolation. This is fulfilled for all directions for the data obtained at lengths above 46 nm. From Fig. 2, it can be seen that above 40 nm, the thermal conductivity does not increase as rapidly as at lower lengths, but the system still has not reached the stable value of the larger than 60 nm lengths. As Evteev *et al.* claimed that the mean free path of copper phonons at 400 K is 4.6 nm, and given that the thermal conductivity values obtained in this study are stable at lengths above 60 nm, it can be assumed that the bulk value of the lattice thermal conductivity has been reached in the presented simulations.[11] This is consistent with experimental measurements of the total thermal transport of copper.[21] By fitting an exponential function to the data, a bulk phonon thermal conductivity of copper of 7.25 ± 0.43 W/mK is obtained, as displayed in Fig. 3(b). If all the data from the different directions are fitted individually, the values obtained for the bulk thermal conductivity are still within the uncertainty of each other. These can be found in the supplementary material, Sec. 3.

Copper is a metal with a small contribution from phonons to the total thermal conductivity at bulk values and room temperature (about 2% with the phonon bulk value estimated from this study and the experimental total thermal conductivity obtained from Wang *et al.*[36]). Hu *et al.*,[19] therefore, predicted that the phonon contribution to the total heat transport increases with decreasing size. Nath *et al.* measured the thermal conductivity of copper thin films and found the thermal conductivity of a 40 nm thick film to be ~83 W/mK at room temperature.[27] This means that at 40 nm, the phonon contribution of copper has increased to about 8%, and our findings, therefore, support the findings of Hu *et al.* However, it should be noted that the thermal transport of the 40 nm film might have been influenced by structural defects and that the ideal thermal conductivity could, in fact, be higher than the reported value.[27] Lugo and Oliva[23] did similar measurements on thin copper films at ambient temperature. Using their reported values, the phonon contribution at 40 nm is estimated to be about 4.9%, with an upper limit of 7.6% and a lower limit of 3.6%, and at 20 nm, the contribution is about 6.7%, with an upper limit of 13.4% and a lower limit of 4.4%, respectively.

The values found for the phonon thermal conductivity in this study are within the range of previous studies done on smaller system sizes. Evteev *et al.* found using Green-Kubo and equilibrium molecular dynamics a thermal conductivity of 6.22 W/mK at 500 K,[11] and also using the Green-Kubo method, Feng *et al.* found values of similar magnitude.[13] Using the NEMD method, Richardson *et al.* found a thermal conductivity of 5.66 W/mK using temperature baths of 300 and 850 K.[30] Using a density functional theory (DFT) method, Wang *et al.* found a thermal conductivity in the range of 6–14 W/mK depending on the exchange correlation, Generalized Gradient Approximation (GGA), or Local-Density Approximation (LDA).[37]

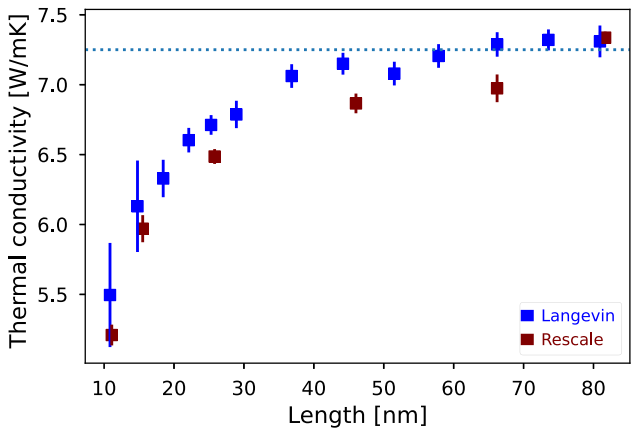

FIG. 4. The lattice thermal conductivities obtained from the NEMD simulations of the [001] direction of copper by two different thermostats, Langevin (blue) and rescale (red), are plotted against the length of the system. The light blue, dotted line represents the obtained thermal conductivity as shown in Fig. 3(b).

© Author(s) 2022

As mentioned in the introduction, the effect of using different thermostats was also investigated, and it is important to note how different the thermal conductivity values are if they are obtained by using the Langevin thermostat to control the thermostated regions. In Fig. 4, the results obtained from the size effect study on [001] from both the Langevin thermostats and the rescale thermostats are plotted. As can be seen, the Langevin thermostat introduced a higher uncertainty to the thermal conductivity, especially at smaller sizes, as well as higher values. This was recently explained by Olarte-Plata and Bresme, who observed a similar difference when studying interfacial thermal conductance.[28] This over-estimation stems from the Langevin thermostat modifying the vibration density of states, leading the distribution to become wider, and decreasing the density of the peaks for their simulation system. This effect is also observed for a pure Si system by Dunn *et al.*, where the difference between the obtained thermal conductivity using Langevin and Nose–Hoover was studied.[10] Our results further highlight the importance of choosing the thermostat in a NEMD simulation with care.

C. Grain boundary conductance

In polycrystalline materials, there will naturally be grain boundaries where grains of different orientations meet. There are numerous types of grain boundaries. The two grain boundaries chosen here, Σ3(112)[110] and Σ5(210)[001], have been widely studied for

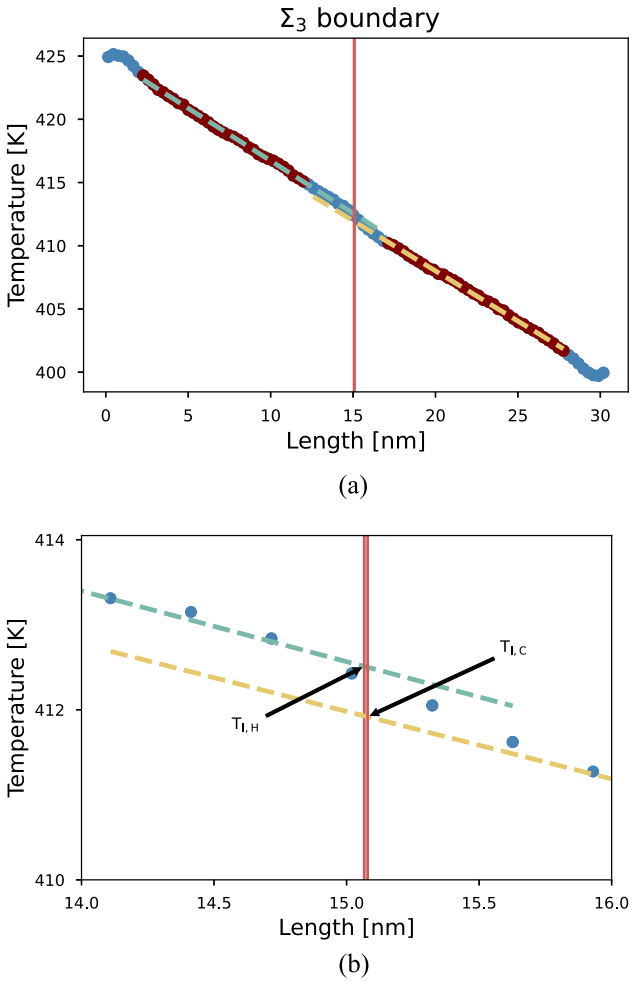

FIG. 5. (a) A typical temperature profile, $T(z)$, from a Σ3 boundary system, where the length of each grain is 15 nm. The minimum and maximum coordinates of the grain boundary, defined as described in Sec. II B, are displayed as red, vertical lines. The maroon-colored regions of the blue temperature profile display where the linear fit was performed, and the green and yellow dashed lines show the extrapolation for the hot and cold interface temperatures, respectively. (b) A magnified view of the interface region, where $T_{I,H}$ and $T_{I,C}$ are defined.

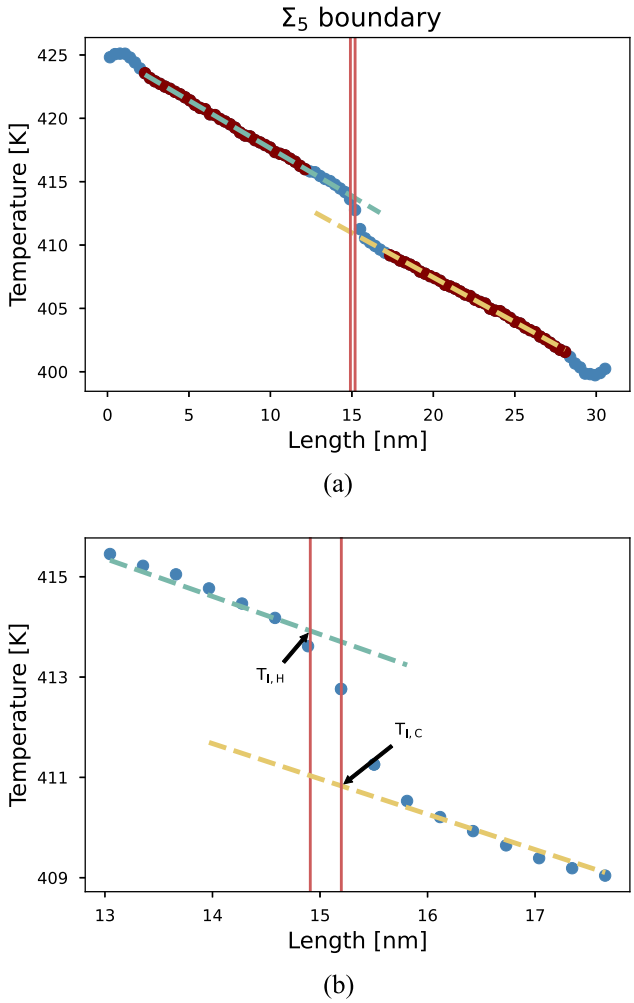

FIG. 6. (a) A typical temperature profile, $T(z)$, from a Σ5 boundary system, where the length of each grain is 15 nm. The minimum and maximum coordinates of the grain boundary, defined as described in Sec. II B, are displayed as red, vertical lines. The maroon-colored regions of the blue temperature profile display where the linear fit was performed, and the green and yellow dashed lines show the extrapolation for the hot and cold interface temperatures, respectively. (b) A magnified view of the interface region, where $T_{I,H}$ and $T_{I,C}$ are defined.

© Author(s) 2022

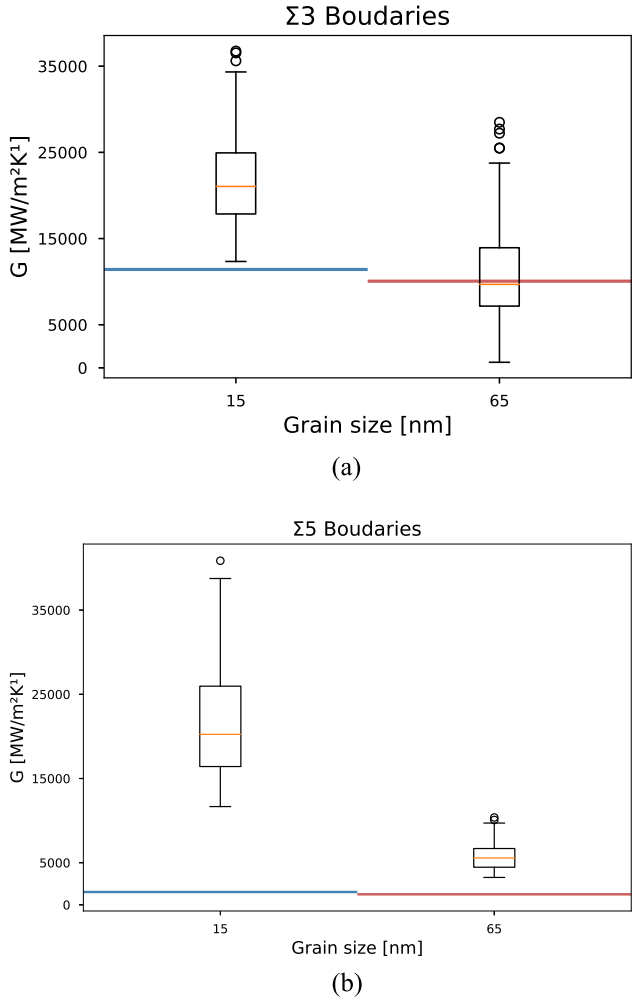

FIG. 7. Box plots for the thermal conductances obtained from the regions not influenced by the thermostats or the boundary from the Σ3 system (a) and the Σ5 system (b). The interfacial conductance obtained at the grain boundary is shown as horizontal lines, the blue line represents the 15 nm sized grain systems, and the burnt orange represents the 65 nm grain systems. The orange line in the boxplot represents the median of the thermal conductances of the given system.

their influence on material properties. Σ3(112)[110] is a twin boundary that has been found to have a very low grain boundary energy for different material systems.[38] The Σ5(210)[001], on the other hand, is a higher energy grain boundary but is still naturally occurring. These two boundaries, therefore, represent a good starting point to study the effect of grain boundaries on phonon thermal transport.

The resulting temperature profiles from the NEMD simulations are displayed in Fig. 5 for the Σ3 boundary and Fig. 6 for the Σ5 boundary, in addition to a zoomed in view of the interface. The method for finding the thermal conductance of the boundaries was outlined in Sec. II B. In order to investigate whether or not the presence of a grain boundary influences the thermal transport, the thermal conductance was additionally calculated between all adjacent points in the regions where the linear regression was made. All the points classified as outliers, according to the criteria given in the following equation:

$$\text{Outlier} : (Q1 - 1.5 \times IQR) \vee (Q3 + 1.5 \times IQR), \tag{8}$$

were removed from the analysis. Here, $Q1$ and $Q3$ are the first and third quartile of the data, respectively, and IQR is the inner quartile range, defined as $Q3 - Q1$. The remaining points are plotted in Fig. 7 as box plots, where the thermal conductance obtained at the interfaces is plotted as well. The results from the simulations are summarized in Table II, where both the thermal conductance of the boundary and adjacent points are included. In addition, the overall thermal conductivity of the systems was calculated, by following the same method as before.

From the data summarized in Table II, there are several observations to be made. First, the Σ3 boundary does not seem to have any influence on the thermal transport of the phonons. The Σ3 boundary in the (15×15) nm grain system is an outlier, whereas the boundary in the (65×65) nm system is well within the variance of the adjacent points. By comparing the overall thermal conductivity obtained for these two systems with systems of comparable size by using the exponential fitting displayed in Fig. 3(b), summarized in Table III, the presence of the boundary does not influence the overall thermal conductivity of the system. As the Σ3 twin boundary is the least disrupting grain boundary a material can obtain, this is reasonable. The uncertainties of all of the thermal conductivities reported, except for the Σ5(210)[001] twist boundary, are quite high. This is likely due to the application of Eq. (5) to cases where there are no well-defined boundaries. This does, however, highlight the fact that the Σ5 boundary has a significant effect on thermal conductance.

The Σ5(210)[001] twist boundary system has a clearly distinguishable thermal conductance at the boundary when compared to the adjacent points, which is apparent from Fig. 7. This is also evident from the vibrational density of state spectra found in the supplementary material, Sec. 3, where the grain boundary region is

TABLE II. Thermal conductances and conductivities for the grain boundary systems.

Boundary	Grain size (nm)	Thermal conductance (MW m^{-2} K^{-1})	Adjacent points (MW m^{-2} K^{-1})	κ_{overall} (W m^{-1} K^{-1})
Σ3	15	11 413 ± 1725	21 879 ± 5448	6.377 ± 0.03
	65	10 055 ± 6426	10 980 ± 5122	7.08 ± 0.09
Σ5	15	1 522 ± 15.75	21 780 ± 6700	5.256 ± 0.53
	65	1 249 ± 78	5 763 ± 1577	7.056 ± 0.05

© Author(s) 2022

TABLE III. The estimated overall thermal conductivity of the single crystal systems of comparable size to the grain boundary systems.

Size (nm)	$\kappa_{overall}$ (MW m^{-2} K^{-1})
30	6.69 ± 0.43
130	7.25 ± 0.43

lacking some order. Still, when comparing the total thermal conductivity to the similar sized single crystals in Table III, the presence of the boundary only influences the thermal conductivity for the smallest system and diminishes as the grain becomes larger. However, as noted in Sec. III B, the effect of the phonons becomes more important for the total thermal conductivity as the system size becomes smaller. It is, therefore, important to include the effect of grain boundaries for these systems.

In addition to the data presented here, one simulation was done for each of the smallest systems with a larger temperature gradient, where the cold thermostat was set to 400 K and the hot thermostat was set to 500 K. The value obtained for the interfacial conductance coincides with the ones obtained for the smaller temperature gradient. These results can be found in the supplementary material, Sec. 3.

IV. CONCLUSION

In electronic devices at the micro- and nanoscale, thermal management is vital. At such small sizes, all details count and need to be taken into careful consideration when devices are designed.

The molecular dynamics simulations done in this study show that there is a clear size effect on phonon thermal transport in copper. This can be shown to follow an exponential function that reaches a plateau at lengths above 60 nm.

At bulk values, the phonons are estimated to contribute 2% of the overall thermal conductivity of copper. However, this contribution increases for decreasing lengths, and at 20 nm, somewhere between 6% and 12% of the total thermal transport can be attributed to phonons.

This increased contribution at smaller sizes further establishes the importance of our second finding, namely that the Σ5(210)[001] twist boundary studied here influences the phonon thermal transport to such a degree that it leads to reduced conductivity of the smaller grain systems. In cases where the systems are of this size, the phonon contribution to the total thermal transport is significant. Therefore, this resistance is of consequence for the thermal performance and needs to be taken into consideration. The low energy Σ3(112)[110] twin boundary does not influence the thermal conductivity of the overall system. Other boundaries should be systematically studied in order to obtain a comprehensive understanding of the effect of grain boundaries on phonon thermal transport.

In this study, we have not observed any discerned effect of crystal orientation on the thermal conductivity of copper. All of these findings are important to bear in mind when designing nano-sized metallic systems for use in thermal transport.

SUPPLEMENTARY MATERIAL

supplementary material is available in a separate PDF and includes the following:

- Uncertainty calculations.
- Vibrational density of state spectra.
- Visualization of the equilibration process and the steady state.
- Individual plots of the thermal conductivity for the different orientations.
- Results from the 15 nm grain boundary systems with a larger temperature gradient.

ACKNOWLEDGEMENTS

This work was financially supported by the Research Council of Norway via the HEFACE project (Grant No. 251068). The computational resources are provided by Norwegian Metacenter for Computational Science (Grant Nos. NOTUR NN9391k and NN9110k).

AUTHOR DECLARATIONS

Conflict of Interest

The authors have no conflicts to disclose.

DATA AVAILABILITY

The data that support the findings of this study are available from the corresponding author upon reasonable request.

REFERENCES

[1] D. E. J. Armstrong, A. J. Wilkinson, and S. G. Roberts, "Measuring anisotropy in Young's modulus of copper using microcantilever testing," J. Mater. Res. **24**(11), 3268–3276 (2009).
[2] A. Basavalingappa, M. Y. Shen, and J. R. Lloyd, "Modeling the copper microstructure and elastic anisotropy and studying its impact on reliability in nanoscale interconnects," Mech. Adv. Mater. Modern Process. **3**(1), 6(2017).
[3] Q. Bian, S. K. Bose, and R. C. Shukla, "Vibrational and thermodynamic properties of metals from a model embedded-atom potential," J. Phys. Chem. Solids **69**(1), 168–181 (2008).
[4] D. Cahill, P. Braun, G. Chen, D. Clarke, S. Fan, K. Goodson, P. Keblinski, W. King, G. Mahan, A. Majumdar *et al.*, "Nanoscale thermal transport. II. 2003–2012," Appl. Phys. Rev. **1**(1), 011305 (2014).
[5] P. Chantrenne, M. Raynaud, and J. L. Barrat, "Study of phonon heat transfer in metallic solids from molecular dynamic simulations," Microscale Thermophys. Eng. **7**(2), 117–136 (2003).
[6] G. Chen, *Nanoscale Energy Transport and Conversion: A Parallel Treatment of Electrons, Molecules, Phonons, and Photons* (Oxford University Press, 2005).
[7] M. S. Daw and M. I. Baskes, "Embedded-atom method: Derivation and application to impurities, surfaces, and other defects in metals," Phys. Rev. B **29**(12), 6443 (1984).
[8] M. S. Daw, S. M. Foiles, and M. I. Baskes, "The embedded-atom method: A review of theory and applications," Mater. Sci. Rep. **9**(7), 251–310 (1993).
[9] N. E. Dowling, "Engineering methods for deformation, fracture and fatigue," in *Mechanical Behavior of Materials* (Pearson, 2007), p. 197.

© Author(s) 2022

[10]J. Dunn, E. Antillon, J. Maassen, M. Lundstrom, and A. Strachan, "Role of energy distribution in contacts on thermal transport in Si: A molecular dynamics study," J. Appl. Phys. **120**(22), 225112 (2016).
[11]A. V. Evteev, L. Momenzadeh, E. V. Levchenko, I. V. Belova, and G. E. Murch, "Molecular dynamics prediction of phonon-mediated thermal conductivity of f.c.c. Cu," Philos. Mag. **94**(7), 731–751 (2014).
[12]D. Faken and H. Jónsson, "Systematic analysis of local atomic structure combined with 3D computer graphics," Comput. Mater. Sci. **2**(2), 279–286 (1994).
[13]B. Feng, Z. Li, and X. Zhang, "Role of phonon in the thermal and electrical transports in metallic nanofilms," J. Appl. Phys. **105**(10), 104315 (2009).
[14]K. Fuchs, "The conductivity of thin metallic films according to the electron theory of metals," Math. Proc. Cambridge Philos. Soc. **34**, 100–108 (1938).
[15]A. Giri and P. E. Hopkins, "A review of experimental and computational advances in thermal boundary conductance and nanoscale thermal transport across solid interfaces," Adv. Funct. Mater. **30**(8), 1903857 (2020).
[16]B. Hafskjold and S. Ratkje, "Criteria for local equilibrium in a system with transport of heat and mass," J. Stat. Phys. **78**(1), 463–494 (1995).
[17]P. Heino, "Thermal conductivity and temperature in solid argon by nonequilibrium molecular dynamics simulations," Phys. Rev. B **71**(14), 144302 (2005).
[18]J. D. Honeycutt and H. C. Andersen, "Molecular dynamics study of melting and freezing of small Lennard-Jones clusters," J. Phys. Chem. **91**(19), 4950–4963 (1987).
[19]Y. Hu, S. Li, and H. Bao, "First-principles based analysis of thermal transport in metallic nanostructures: Size effect and Wiedemann-Franz law," Phys. Rev. B **103**(10), 104301 (2021).
[20]C. Huang, Q. Wang, and Z. Rao, "Thermal conductivity prediction of copper hollow nanowire," Int. J. Therm. Sci. **94**(C), 90–95 (2015).
[21]F. Kelemen, "Pulse method for the measurement of the thermal conductivity of thin films," Thin Solid Films **36**(1), 199–203 (1976).
[22]C. Kittel, *Introduction to Solid State Physics*, 8th ed. (John Wiley & Sons, 2005).
[23]J. M. Lugo and A. I. Oliva, "Thermal diffusivity and thermal conductivity of copper thin films at ambient conditions," J. Thermophys. Heat Transfer **30**(3), 481–489 (2016).
[24]A. F. Mayadas and M. Shatzkes, "Electrical-resistivity model for polycrystalline films: The case of arbitrary reflection at external surfaces," Phys. Rev. B **1**(4), 1382 (1970).
[25]A. McGaughey and M. Kaviany, "Thermal conductivity decomposition and analysis using molecular dynamics simulations. Part I. Lennard-Jones argon," Int. J. Heat Mass Transfer **47**(8-9), 1783–1798 (2004).
[26]Y. Mishin, M. J. Mehl, D. A. Papaconstantopoulos, A. F. Voter, and J. D. Kress, "Structural stability and lattice defects in copper: *Ab initio*, tight-binding, and embedded-atom calculations," Phys. Rev. B **63**(22), 224106 (2001).
[27]P. Nath and K. L. Chopra, "Thermal conductivity of copper films," Thin Solid Films **20**(1), 53–62 (1974).
[28]J. D. Olarte-Plata and F. Bresme, "The impact of the thermostats on the non-equilibrium computer simulations of the interfacial thermal conductance," Mol. Simul. **48**(1), 87–98 (2022).
[29]S. Plimpton, "Fast parallel algorithms for short-range molecular dynamics," J. Comput. Phys. **117**(1), 1–19 (1995).
[30]C. F. Richardson and P. Clancy, "Contribution of thermal conductivity to the crystal-regrowth velocity of embedded-atom-method-modeled metals and metal alloys," Phys. Rev. B **45**(21), 12260 (1992).
[31]S. Sæther, M. Falck, Z. Zhang, A. Lervik, and J. He, "Thermal transport in polyethylene: The effect of force fields and crystallinity," Macromolecules **54**(13), 6563–6574 (2021).
[32]D. P. Sellan, E. S. Landry, J. E. Turney, A. J. H. McGaughey, and C. H. Amon, "Size effects in molecular dynamics thermal conductivity predictions," Phys. Rev. B **81**(21), 214305 (2010).
[33]E. H. Sondheimer, "The mean free path of electrons in metals," Adv. Phys. **50**(6), 499–537 (2001).
[34]N. Stojanovic, D. Maithripala, J. Berg, and M. Holtz, "Thermal conductivity in metallic nanostructures at high temperature: Electrons, phonons, and the Wiedemann-Franz law," Phys. Rev. B **82**(7), 075418 (2010).
[35]A. Stukowski, "Visualization and analysis of atomistic simulation data with OVITO-the open visualization tool," Modell. Simul. Mater. Sci. Eng. **18**(1), 015012 (2010).
[36]Y. Wang, X. Ruan, and A. K. Roy, "Two-temperature nonequilibrium molecular dynamics simulation of thermal transport across metal–nonmetal interfaces," Phys. Rev. B **85**(20), 205311 (2012).
[37]Y. Wang, Z. Lu, and X. Ruan, "First principles calculation of lattice thermal conductivity of metals considering phonon–phonon and phonon–electron scattering," J. Appl. Phys. **119**(22), 225109 (2016).
[38]X. Wu, Y.-W. You, X.-S. Kong, J.-L. Chen, G.-N. Luo, G.-H. Lu, C. Liu, and Z. Wang, "First-principles determination of grain boundary strengthening in tungsten: Dependence on grain boundary structure and metallic radius of solute," Acta Mater. **120**, 315–326 (2016).

© Author(s) 2022